⊗ANS

Methodology for Generating Covariance Data of Thermal Neutron Scattering Cross Sections

Chris W. Chapman, [a]* Goran Arbanas,[a] Alexander I. Kolesnikov,[b] Luiz Leal,[c] Yaron Danon,[d] Carl Wendorff,[d] Kemal Ramić,[d] Li Liu,[d] and Farzad Rahnema[e]

[a]*Oak Ridge National Laboratory, Nuclear Data and Criticality Safety, Reactor and Nuclear Systems Division, Oak Ridge, Tennessee 37831*
[b]*Oak Ridge National Laboratory, Neutron Scattering Division, Oak Ridge, Tennessee 37831*
[c]*Institut de Radioprotection et de Sûréte Nucléaire, 31, avenue de la division Leclerc, Fontenay-aux-Roses 92260, France*
[d]*Rensselaer Polytechnic Institute, Gaerttner LINAC Center, 3021 Tibbits Avenue, Troy, New York 12180*
[e]*Georgia Institute of Technology, Nuclear and Radiological Engineering Department, 770 State Street, Atlanta, Georgia 30332*

Abstract — *This paper details and implements a framework for evaluating thermal neutron scattering cross sections that provide $S(\alpha, \beta)$ data and covariance data for hydrogen in light water. This methodology involves perturbing model parameters of molecular dynamics potentials and fitting the simulation results to experimental data. The framework is general and can be applied to any material or simulation method. The fit is made using the Unified Monte Carlo method to experimentally measure double-differential scattering cross sections of light water at the Spallation Neutron Source at Oak Ridge National Laboratory. Mean values and covariance data were generated for model parameters, phonon density of states, double-differential cross sections, and total scattering cross sections. These posterior parameter values were very similar to their prior values with a maximum relative error of 0.54%. This falls within in the Unified Monte Carlo–calculated uncertainties on the order of 2.7%. Additionally, posterior double-differential cross sections agree favorably with ENDF/B-VIII.0 cross sections. The new thermal scattering law was tested by comparing it against benchmarks from the International Criticality Safety Benchmark Evaluation Project Handbook, which showed a slight improvement over the ENDF/B-VIII.0 library. Additionally, the covariance matrix of the phonon density of states was validated to confirm that the spread of k_{eff} from the density of states used to generate the covariance matrix was similar to the spread of k_{eff} from the density of states of the sampled covariance matrix.*

Keywords — *Thermal neutron scattering, Unified Monte Carlo, uncertainty quantification.*

Note — *Some figures may be in color only in the electronic version.*

*E-mail: chapmancw@ornl.gov

I. INTRODUCTION

Accurate nuclear data are paramount for a wide range of applications, including reactor simulations, criticality safety, and nonproliferation concerns. With these data, a fundamental understanding of the underlying

uncertainties and covariances is crucial for better quantifying uncertainties. Although these data are well known and available for resolved resonance, unresolved resonance, and fast energy regions, there is not yet an agreed upon method for generating and disseminating covariance data for thermal neutron scattering data.

Previous efforts to quantify covariances in thermal neutron scattering have involved Monte Carlo sampling from a phonon density of states,[1] analytical fitting of LEAPR (an NJOY module) (Ref. 2) parameters to data,[3,4] or analytical fitting of molecular dynamics (MD) model parameters to data.[5] The latter two studies explicitly state that although they provided covariances for their respective parameters, they did not change the values of their parameters.

This work seeks to expand upon previous efforts by optimizing model parameters so that the resulting parameters yield a better fit to experimental data. Specifically, this methodology will employ the Unified Monte Carlo (UMC) method to fit the TIP4P/2005f model parameters of light water simulated using GROMACS (Ref. 6) and MCNP6.2 (Ref. 7) to double-differential scattering cross sections measured at the Oak Ridge National Laboratory (ORNL) Spallation Neutron Source (SNS). This contrasts with previous works that constrained the fit to the phonon density of states[4] or the average cosine of the scattering angle and total cross section.[5]

Although the method can generate covariance matrix data for any property used in the evaluation procedure [including $S(\alpha, \beta)$], this work focuses on generating covariance data for the phonon density of states. While there are several groups looking into thermal scattering covariances [e.g., the General Nuclear Database Structure and Working Party on International Nuclear Data Evaluation Cooperation (WPEC) subgroup 42/44/48], there is no agreed-upon method for generating or storing thermal scattering covariance data. This work will serve as a test case to determine if this information can be stored in the phonon density of states for materials where the thermal scattering law is calculated solely from the phonon density of states. This will be tested against benchmarks from the International Criticality Safety Benchmark Evaluation Project (ICSBEP) Handbook[8] by comparing the spread of the results used to generate the covariance matrix with the results used when the matrix is sampled.

A brief discourse on the theory behind thermal neutron scattering and the UMC method is discussed in Sec. II. Fundamental water properties, a description of the TIP4P/2005f model, and the experimental data are discussed in Sec. III. A description of how the UMC model is employed in this work and the associated results are given in Sec. IV. Results comparing the newly generated library and the ENDF/B-VIII.0 library against integral benchmarks, as well as results from testing the covariance matrix are provided in Sec. V, and some concluding thoughts are provided in Sec. VI.

II. THEORY

II.A. Thermal Neutron Scattering

At small-incident neutron energies (<1 eV), the de Broglie wavelength of the neutron becomes comparable to the interatomic distances in solids and liquids. At higher-incident neutron energies the effects of the binding energies of the target molecule or crystal can be neglected, but they must be accounted for in the thermal neutron energy range. This derivation has been expounded upon in other works (e.g., Price and Fernandez-Alonso[9] and Squires[10]), so only a brief overview is detailed in this section.

The double-differential cross section can be represented by Eq. (1):

$$\frac{d^2\sigma}{dE_f d\Omega} = \frac{\sigma_b}{4\pi k_B T} \sqrt{\frac{E_f}{E_i}} e^{-\beta/2} S(\alpha, \beta) \,, \tag{1}$$

where

$$\begin{aligned}
\sigma_b &= \text{bound scattering cross section} \\
k_B &= \text{Boltzmann constant} \\
T &= \text{temperature} \\
E_{i,f} &= \text{incident and final energies of the neutron,} \\
&\quad \text{respectively} \\
S(\alpha, \beta) &= \text{thermal scattering law.}
\end{aligned}$$

The bound scattering cross section is related to the free scattering cross section by

$$\sigma_b = \left(\frac{A+1}{A}\right)^2 \sigma_f \,, \tag{2}$$

where A is the ratio of the mass of the scattering atom to the mass of the neutron, and σ_f is the free atom scattering cross section. In Eq. (1), α is the unitless variable for momentum, and β is the unitless variables for energy transfer; both are defined by Eq. (3):

$$\alpha = \frac{\hbar^2 q^2}{2M k_B T} \tag{3}$$

and

$$\beta = \frac{-E}{k_B T} \ ,$$

where

E = energy transfer between the neutron and the target nucleus

M = mass of the scattering atom

q = wave vector transfer.

The wave vector transfer is defined by

$$\hbar q = k_i - k_f \ , \tag{4}$$

where $k_{i,f}$ are the wave vectors of the incoming and outgoing neutron, respectively, and $\hbar q$ is the momentum transfer between the neutron and the target nucleus. The thermal scattering law is defined by the dynamic structure factor by

$$S(\alpha, \beta) = k_B T e^{-E/(2k_B T)} S(q, E), \tag{5}$$

where $S(q, E)$ is the dynamic structure factor. From here, Van Hove[11] states that this term can be defined as the Fourier transform of the intermediate structure factor by

$$S(q, E) = \frac{1}{2\pi\hbar} \int_{-\infty}^{\infty} F(q, t) e^{-iEt/\hbar} dt \ , \tag{6}$$

where $F(q, t)$ is the intermediate structure factor.

Thermal neutron scattering can be split into two separate categories: coherent and incoherent scattering. Coherent scattering occurs when the neutron wavelength interacts with multiple nuclei simultaneously. This causes interference effects and is most often seen in crystalline materials, such as graphite. Incoherent scattering occurs when the neutron scatters off of only one nucleus, causing no interference effects between other atoms in the sample. This is more prevalent in hydrogenous materials, including water. While it is possible for a material to contain both coherent and incoherent scattering (e.g., graphite has coherent elastic and incoherent elastic features), because of the relative difference in coherent versus incoherent scattering cross sections of hydrogen (1.7 versus 80.2 b), the incoherent approximation can be used, which assumes that there is no coherent scattering in the final double-differential scattering cross section. With this approximation, the intermediate structure factor can be defined by Gurevich and Tarasov[12]:

$$F(q,t) = \exp$$
$$\left[-\frac{q^2}{2} \int_0^{\infty} d\omega \frac{g(\omega)}{\omega} \left\{ \coth\left(\frac{\hbar\omega}{2k_B T} \right) (1 - \cos(\omega t)) - i\sin(\omega t) \right\} \right] \ , \tag{7}$$

where $g(\omega)$ is the generalized frequency distribution. The generalized frequency distribution is defined here as

$$g(\omega) = \int_0^{\infty} dt \cos(\omega t) \text{vacf}(t) \ , \tag{8}$$

where $\text{vacf}(t)$ is the velocity autocorrelation function. The generalized frequency distribution can be determined experimentally[13] or computationally from MD simulations.[14]

II.B. Unified Monte Carlo

In the resolved, unresolved, and fast-energy regions, covariance data are often evaluated using the generalized least-squares (GLS) method.[15] This method is robust and sufficient for those energy regions but requires sensitivities to calculate the covariance matrix. To use GLS for this framework, the sensitivities must be calculated, which would require either modifying the MD code[16] or calculating the derivatives numerically, which would be prohibitively computationally expensive. Because of this limitation, a different model is needed to evaluate thermal scattering law data.

The use of Monte Carlo methods for estimating uncertainties in cross sections derived from nuclear models was first detailed in Ref. 17. This would eventually lead to the UMC method, first described by Smith[18] and Capote and Smith,[19] that follows from the Bayes theorem and the Principle of Maximum Entropy.[20] In the following description, values with a c index represent computational simulation results, and values with an E index represent experimental results. If an experiment containing n data points is represented by y_E, its associated covariance matrix is represented by V_E, the simulation results containing m data points are represented by x_c, and its associated covariance matrix is V_c, then the Bayes theorem gives the posterior probability density function (PDF) as

$$p(x) = \text{N} L(y_E, V_E | x) p_o(x | x_c, V_c) \ , \tag{9}$$

⊗**ANS**

where

N = normalization constant

$L(y_E, V_E|x)$ = likelihood PDF

$p_o(x|x_c, V_c)$ = prior PDF.

There are two variants of the UMC method: UMC-G (Ref. 19) and UMC-B (Ref. 21). A more complete description of the methods can be found in Ref. 22, and will be summarized here. UMC-G provides an analytic expression to Eq. (9), which can be sampled using a Metropolis-Hastings algorithm to provide the best estimate of the result. The primary drawback to using this algorithm in this work is that each sampling requires running MD simulations that take on the order of hours to run, and convergence is usually seen only after 10^5 iterations. The primary advantage of UMC-B is that mean values of the simulation data x_c and its associated covariance matrix V_c are not calculated. Instead, a collection of scalar weights ω_k are calculated for each independent simulation k by

$$\omega_k = \exp\left\{ -\frac{1}{2}\left[(y_k - y_E)^T \cdot V_E^{-1} \cdot (y_k - y_E)\right]\right\}, \tag{10}$$

where $y_k = f(x_{ck})$ and x_{ck} are the simulation data from simulation k, and $f(x_{ck})$ is the function needed to transform the simulation data to simulated experimental data. In this case, the code simulates the dynamic structure factor, and $f(x)$ is the process of transforming it into double-differential cross sections to compare against the experimental data. Once these weights are calculated, the mean and covariance values can be calculated by

$$\langle x_i \rangle = \lim_{K \to \infty} \frac{\sum_{k=1}^{K} x_{ik}\omega_k}{\sum_{k=1}^{K} \omega_k} \tag{11}$$

and

$$\langle V \rangle_{i,j} = \lim_{K \to \infty} \frac{\sum_{k=1}^{K} x_{ik}x_{jk}\omega_k}{\sum_{k=1}^{K} \omega_k} - \langle x_i \rangle \langle x_j \rangle . \tag{12}$$

In Eqs. (11) and (12), the variable x_{ik} can be any variable from simulation k and does not necessarily need to be the same value used to calculate the weight.

III. WATER

III.A. Water Model

Water is a difficult material to model computationally. There are several reasons for this that are detailed elsewhere,[23] and can range from the creation of extensive hydrogen bonding networks, to dimer interactions, to nonadditive effects due to large dipole and the polarizability of water. Depending on the chosen computational simulation method (i.e., classical versus *ab initio* MD), the models can vary between empirical models fitted to experimental data or defined using potential wave functions of the corresponding atoms in the molecule. This study will focus on classical MD and will not take into account noncontinuous motions of water molecules at the picosecond timescale (jump-diffusion). These empirical models are defined by the number of sites that are simulated in an MD simulation. Each site represents an interaction point that can interact with another site. An example configuration of a four-site model is shown in Fig. 1.

The model used in this study is the TIP4P/2005f potential.[25] This model was chosen in part because it offers a favorable tradeoff between model complexity and the accuracy of the phonon density of states, and also because it is the model on which the ENDF/B-VIII.0 evaluation of light water is based.[26] The model is a four-site model in which the fourth site (labeled M in Fig. 1) is called a dummy site. In this case, the electric charge of the oxygen atom is stored on the dummy particle, and the mass of the oxygen atom is stored at the oxygen atom. This improves the electrostatic distribution around the water molecule. Eight parameters from this model will be varied using UMC.
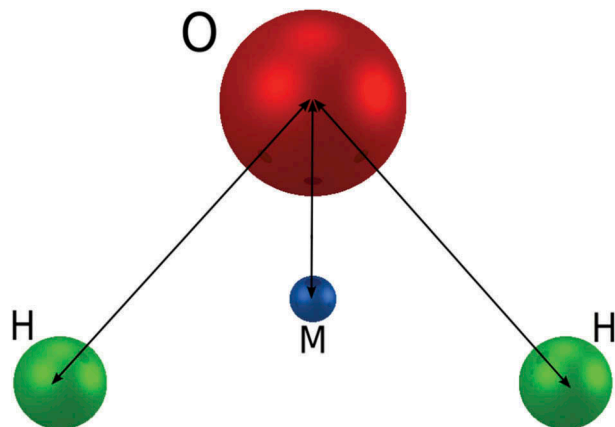

Fig. 1. Four-site water model.[24]

The model is governed by a potential function $V(r)$ defined by

$$V(r) = V_c(r) + V_{LJ}(r) + V_{bs}(r) + V_\theta(r) \ , \qquad (13)$$

where

$V_c(r)$ = Coulomb potential

$V_{LJ}(r)$ = Lennard-Jones potential

$V_{bs}(r)$ = bond stretching term

$V_\theta(r)$ = bond angle term.

The first two terms can be considered intermolecular terms, and the latter two can be considered intramolecular terms.

The Coulomb potential describes how charged particles interact with each other, and it is defined as

$$V_c(r) = \frac{1}{4\pi\epsilon_o} \frac{q_i q_j}{\epsilon_r r_{ij}} \ , \qquad (14)$$

where

ϵ_o = permittivity of free space

ϵ_r = dielectric constant

$q_{i,j}$ = charges of particles i and j, respectively

$r_{i,j}$ = distance between particles i and j.

Because the potential extends over all space, MD codes will cut off these Coulombic interactions at a given length. Beyond this length, long-range electrostatics are handled using the particle-mesh Ewald method.[27]

The Lennard-Jones potential describes how neutrally charged particles interact with one another. Because the oxygen atoms contain no charge, this is necessary for describing how oxygen atoms of different water molecules interact. This is defined by

$$V_{LJ}(r) = 4\epsilon \left(\left(\frac{\sigma}{r_{ij}}\right)^{12} - \left(\frac{\sigma}{r_{ij}}\right)^{6} \right) \ , \qquad (15)$$

where ϵ is the depth of the potential well, and σ is the finite distance between particles i and j where the potential changes from repulsive to attractive. The r^{-12} term describes the Pauli repulsion at short ranges due to overlapping electron orbitals, and the r^{-6} term describes the attraction at long ranges due to the van der Waals force.

The bond-stretching term describes the strength of the bond between the hydrogen and oxygen atoms and how the atoms vibrate along the bond length. The TIP4P/

2005f model uses an anharmonic function called the Morse potential because it yields better agreement with the higher-energy stretching bands and is less computationally intensive than a quartic function. This Morse potential is defined as

$$V_{bs}(r) = D_r \left[1 - e^{-\beta(r_{ij}-b_0)^2} \right] \ , \qquad (16)$$

where

D_r = depth of the potential well

β = steepness of the well

b_0 = equilibrium length between the hydrogen and oxygen atoms within the same molecule.

The bond angle term describes how the hydrogen atoms bend in relation to the oxygen atom. The bond angle is given by the following harmonic function:

$$V_\theta(r) = \frac{1}{2} K_\theta \left(\theta_{ijk} - \theta_0 \right)^2 \ , \qquad (17)$$

where

K_θ = bond strength

θ_{ijk} = angle between atoms i, j, and k

θ_0 = equilibrium angle between atoms i, j, and k.

All of the parameters that will be modified and their published values from Gonzlez and Abascal[25] are shown in Table I. The parameters are the same as those described in Eqs. (15), (16), and (17), with the addition of the d_0 parameter, which describes the distance between the oxygen atom and the dummy particle site.

III.B. Experiment

The experimental data were gathered from the Fine-Resolution Fermi Chopper[28] (SEQUOIA) beamline at the ORNL SNS in 2012 by a research group from the Rensselaer Polytechnic Institute. SEQUOIA is a direct geometry time-of-flight chopper spectrometer in which an incident energy is specified and a spectra of final energies and scattering angles are measured. This is performed using a Fermi Chopper, which has a series of curved, closely spaced neutron-absorbing blades (slit package) held together by a rotor that spins around a vertical axis in the path of the beam. The Fermi Chopper can rotate at a specific frequency, 60 to 600 Hz, to allow only neutrons at a specific energy to pass. The neutrons then hit the sample of water, which was encapsulated within a 0.1-mm-thick aluminum flat

container with a 50×50 mm^2 cross sectional area. This thickness was chosen to reduce the effects of multiple neutron scattering. The sample size of the aluminum container coincided with the cross-sectional area of the neutron beam, as the equipment is designed to have the sample in the center of the beam. The uncertainties in the sample geometry are negligible compared with other sources of experimental uncertainty, which are on the order of 1% to 5%.

The scattered neutrons are then detected by one of the detectors, which tally the neutrons' arrival time so the scattered energy can be calculated. The detector bank covers scattering angles from -30 to 60 deg in the horizontal plane and ± 18 deg in the vertical direction. The collected inelastic neutron scattering (INS) data were transformed from the time-of-flight and instrument coordinates to the dynamic structure factor $S(q, E)$ as defined in Eq. (6) and corrected for the detectors' efficiency by using white-beam vanadium data. Monochromatic vanadium normalization of the data was not performed. The spectra from the empty aluminum container were also measured at the same conditions and subtracted from the water data to remove the effect of the neutron scattering from the container.

The data were collected at incident energies of 55, 160, 250, 600, 1000, 3000, and 5000 milli-electron volts (meV) between scattering angles of 3 to 58 deg and grouped with 1-deg increments. The energy resolution for the double-differential cross sections with the used Fermi Chopper 1 at the elastic line (energy transfer $E = 0$) and at $E = 0.9E_i$ are given in Table II. These energies correspond to the full-width half-maximum of the Gaussian resolution function for each experiment at the given value (at $E = 0$ and $E = 0.9E_i$). Each experiment was performed at 300 K.

TABLE I

TIP4P/2005f Parameters*

Parameter (unit)	Value
β (nm^{-1})	22.87
b_0 (nm)	0.09419
d_0 (nm)	0.01546
D_r (kJ/mol)	432.581
ϵ (kJ/mol)	0.7749
K_θ [kJ/(mol rad^2)]	367.810
σ (nm)	0.31644
θ_0 (deg)	107.4

*As reported in Ref. 25 and detailed in paper.

IV. FRAMEWORK AND RESULTS

IV.A. Framework Overview

The MD simulations were run using GROMACS and were divided into four steps. First, a system of 512 water molecules in a cube with sides of 2.407 nm was minimized using the steepest descent method over 500 000 steps, and the positions of the atoms were changed so that the total force in the system was minimized. Then, the system was simulated for 100 ps with a 0.1-fs time step in a canonical (NVT) ensemble in which the number of molecules, volume, and temperature were held constant. The temperature was coupled using a Nose-Hoover extended ensemble. Next, an isothermal-isobaric simulation (NPT), in which the number of molecules, pressure, and temperature are held constant, was performed for 1 ns with a 0.1-fs time step. Again, the temperature was coupled using a Nose-Hoover extended ensemble, and the pressure was coupled using the Parrinello-Rahnam scheme in which the pressure coupling of the box vectors was subject to the equations of motion. Finally, a microcanonical ensemble (NVE), in which the number of molecules, volume, and total energy are held constant, was performed for 100 ps with a 0.1-fs time step. In this step, the MD frames were saved every 0.4 fs. In all of these runs, a cutoff length of 0.8 nm was used for the electrostatic and Lennard-Jones potentials, and periodic boundary conditions were assumed so that, for example, particles leaving the system in the $+x$ direction were simulated as entering in the system from the $-x$ direction.

In this work, the model parameters were randomly generated using the Latin hypercube sampling method to ensure that the entire phase space of parameters was appropriately sampled. The parameters sampled in this work are limited to only the parameters in the TIP4P/ 2005f parameter set. There has been work to modify other physical properties of water (e.g., the free atom scattering cross section[4]), but those will not be explored in this analysis. A total of 2048 samples were generated with a maximum value of any individual parameter of $\pm 5\%$ of the published value of that parameter.

The MD simulations were initialized assuming a random orientation of water molecules and were randomly reoriented if the configuration was incompatible with the parameter set (i.e., if the MD simulation failed). Several physical properties were calculated from the resulting trajectories, including dielectric constant, relative static dielectric constant, density, diffusion

TABLE II

Fermi Chopper 1 Energy Resolution*

E_i	55	160	250	600	1000	3000	5000
$E = 0$	3.2	9.5	13	34	74	360	850
$E = 0.9E_i$	0.8	2.0	3.0	7.0	15	80	200

*All units are in milli-electron volts.

coefficient, isothermal compressibility, and heat capacity, to further verify that the simulations produced physically realistic results. Additionally, the velocity autocorrelation functions for hydrogen and oxygen were calculated so that the phonon density of states could be calculated using Eq. (8). With this density of states, a thermal scattering law was calculated using an in-house program written for this project[29] that evaluates Eqs. (6) and (7).

Of the 2048 samples, 1615 ran successfully, as the remaining 433 parameter sets caused the MD simulations to crash. These crashes occurred even after repeated reorientation of the initial water molecule configuration, meaning that these 433 parameter sets were not possible to simulate. From the 1615 successful runs, 250 simulations were used to calculate the UMC weights. These simulations correspond to the runs where the calculated densities and diffusion coefficients were within 15% and 30% of their experimentally measured values, respectively. Values with larger deviations away from the experimental values resulted in smaller values for the UMC weights, and thus made a small contribution to the UMC-calculated mean and covariances. The density and diffusion coefficients were chosen because they are accurately known and have the highest correlation to a correct phonon density of states. To better replicate the experimental setup, a simplified model of the SEQUOIA spectrometer detector was modeled in MCNP6.2, in which a monoenergetic beam of neutrons was fired at a sample of water and the scattering results were tallied at rings meant to represent how SEQUOIA tallied the scattering events.

The choice to down-select from 1615 to 250 parameter sets is twofold. From a theoretical perspective, as the large ensemble of parameter sets was chosen to ensure a proper sampling of phase space, it was expected that some simulations would run to completion while providing unrealistic thermophysical properties. This down-selecting served as a way to ensure that the whole phase space of the TIP4P/2005f parameters leading to physically reasonable properties of water was covered while ensuring the UMC-calculated uncertainties were realistic. From a practical standpoint, running 11 305 MCNP runs (the number required if we had

selected all 1615 successfully run simulations) would be computationally prohibitive. Additionally, including the 1365 omitted ensembles in the UMC analysis would not have affected the presented results, as their UMC-generated weights from Eq. (10) would so small as to not make a meaningful contribution to the UMC mean or covariance values.

After the SEQUOIA resolution function was applied, the resulting double-differential scattering cross sections were used to calculate the UMC weights using Eq. (10), where y_k is the calculated double-differential scattering cross section, y_E is the experimental double-differential scattering cross section, and V_E is the experimental covariance matrix. This covariance matrix was assumed to contain no cross correlations, making it a diagonal matrix of the variance of the experimental results. In addition to the double-differential scattering cross section, the calculated diffusion coefficient and density were also included in the generation of the UMC weights since they were determined to be critical for achieving good agreement between simulated and experimental results.

A flow chart detailing the framework is shown in Fig. 2. The weights were computed according to Eq. (10) by scaling the value of χ^2 in order for posterior mean values and their uncertainties to be deemed in harmony with the double-differential data.[30] The weights calculated for the UMC ensemble of the TIP4P/2005f parameter sets in this work are plotted in Fig. 3 and are listed in the supplemental material along with the corresponding TIP4P/2005f parameter sets.

A plot of the UMC weights sorted from largest to smallest is shown in Fig. 3. The weights are normalized such that the average value equals 1. This was done for convenience, as it does not affect the calculations associated with these weights. The larger value weights indicate a better agreement with the differential data, density, and diffusion coefficient, meaning that they will have a larger impact on the UMC-averaged values. These weights were then used to calculate the mean values and covariance matrices for the model parameters, physical properties density of states, and double-

differential scattering cross sections. The mean value and variance of the dynamic structure factor were also calculated.

IV.B. Model Parameters and Thermophysical Properties

Using the UMC weights, the average values of the updated TIP4P/2005f model parameters and the tabulated physical properties, along with their comparison with the values calculated from Gonzlez and Abascal,[25] were calculated and are shown in Tables III and IV, respectively. The spread of the 250 values are shown in Figs. 4 and 5. Their corresponding correlation matrix was calculated using

$$C_{i,j} = \frac{V_{i,j}}{\sqrt{V_{i,i}V_{j,j}}} \ , \tag{18}$$

where $V_{i,j}$ is the covariance matrix defined by Eq. (12), which is shown in Fig. 6. The correlation matrix of the TIP4P/2005f parameters is shown in Table V.
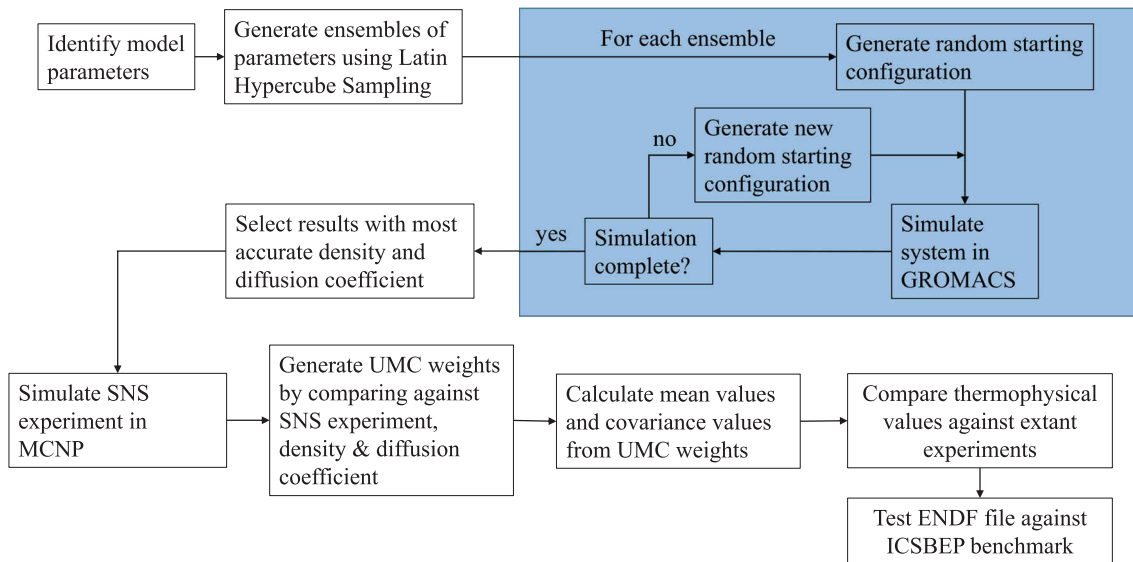
Fig. 2. Flow chart detailing outlined thermal neutron scattering evaluation methodology.
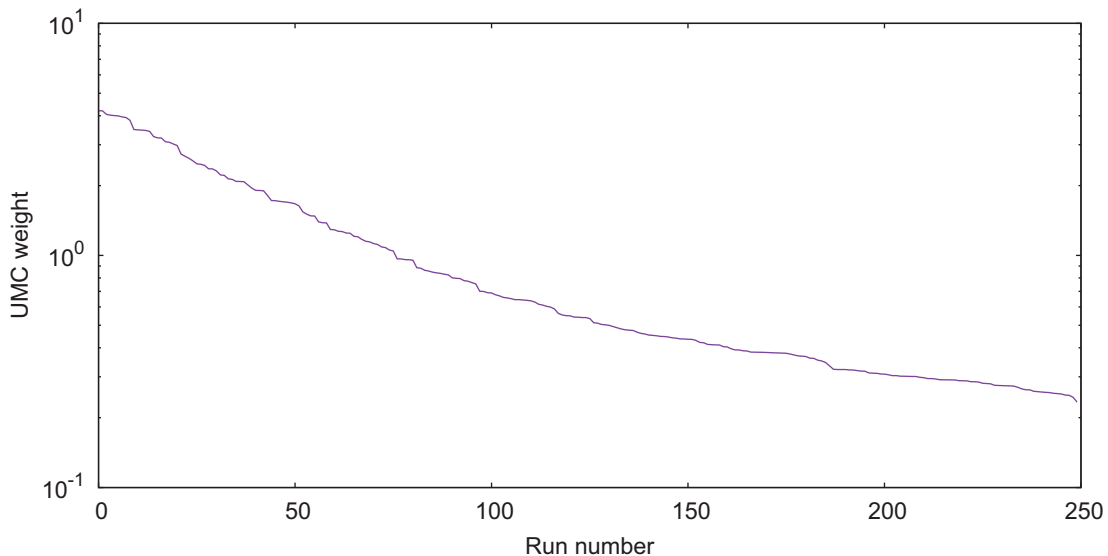
Fig. 3. Sorted UMC weights calculated using Eq. (11).

TABLE III

UMC-Updated TIP4P/2005f Parameters

Parameter	UMC Mean Value	UMC Uncertainty	Published Value[a]	Relative Error
β	2.291E+01	6.672E−01 (2.91%)	2.287E+01	0.15%
b_0	9.441E−02	2.707E−03 (2.87%)	9.419E−02	0.23%
d_0	1.545E−02	4.664E−04 (3.02%)	1.546E−02	0.08%
D_r	4.34152E+02	1.23567E+01 (2.85%)	4.32581E+02	0.36%
ϵ	7.717E−01	2.141E−02 (2.77%)	7.749E−01	0.42%
K_θ	3.6695E+02	1.0209E+01 (2.78%)	3.6781E+02	0.23%
σ	3.1679E−01	7.6056E−03 (2.40%)	3.1644E−01	0.11%
θ_0	1.068E+02	3.087E+00 (2.89%)	1.074E+02	0.54%

[a]Reference 25.

TABLE IV

UMC-Updated Thermophysical Properties

Property (unit)	UMC Mean Value	UMC Uncertainty	Published Value	Exp. Value
p (Debye)	2.299E+00	1.597E−01 (6.949%)	2.319E+00	2.95E+00
ϵ_r (N/A)[a]	5.518E+01	1.230E+01 (22.29%)	5.53E+00	7.84E+01
ρ (g cm^{-3})	9.961E−01	7.165E−02 (7.193%)	9.977E−01	9.97E−01
D_s (10^9 m^2 s^{-1})	2.241E+00	3.644E−01 (16.26%)	1.93E+00	2.27E+00
κ_T (10^4 MPa^{-1})	4.953E−01	5.402E−02 (10.91%)	4.46E−01	4.95E−01

[a]N/A = Not applicable. Exp. = Experimental.

The UMC analysis changed the mean values of the TIP4P/2005f parameters as expected, but none of the values were significantly changed. Although the UMC uncertainties might appear small, the intent of running a large number of simulations and then discarding those with unphysical values of density and diffusivity was precisely a way to ensure that the 250 parameter sets used in the final UMC analysis completely covered the physical range of the TIP4P/2005f parameters, thus yielding realistic uncertainties of the TIP4P/2005f parameters.[a] The values all have a relative error of less than 1%, and most are below 0.25%. These results were expected because the TIP4P/2005f parameter set was already tuned to give agreeable results when compared with thermophysical properties. This analysis effectively tuned these parameters to the double-differential cross section of water. The frequency plots provide some insight into which parameters were chosen from the original 1615 parameter sets for further analysis. The parameters were originally sampled assuming a uniform distribution, and although some of the parameters show a somewhat uniform distribution (specifically β and d_o), some of them exhibit a noticeable trend. Specifically, σ

appears to be centrally peaked, and θ_o shows a decreasing frequency with increasing angle.

Neither the dipole moment nor the relative static dielectric constant are accurately calculated by the TIP4P/2005f potential or the updated parameter set. This is most likely because the TIP4P/2005f model is a four-site model, and higher site models tend to calculate these properties more accurately. This is an active area of research, and other types of water models (such as polarizable potentials, or use of *ab initio* MD) might yield more accurate results for these values.

The diffusion coefficient and isothermal compressability are calculated to be much closer to the experimental

---

[a]This may be illustrated by considering the pitfalls of random sampling of the TIP4P/2005f parameters from a too narrow range of values, such that all MD simulations would be acceptable but would yield unrealistically small uncertainties. Conversely, sampling from a much larger range of TIP4P/2005f parameters would yield a much smaller fraction of acceptable runs. Consequently, we have sampled over a range of parameter values that would still yield a sufficient number of acceptable runs, i.e., 250, for a statistically meaningful UMC analysis, but without unduly restricting the range of parameters.
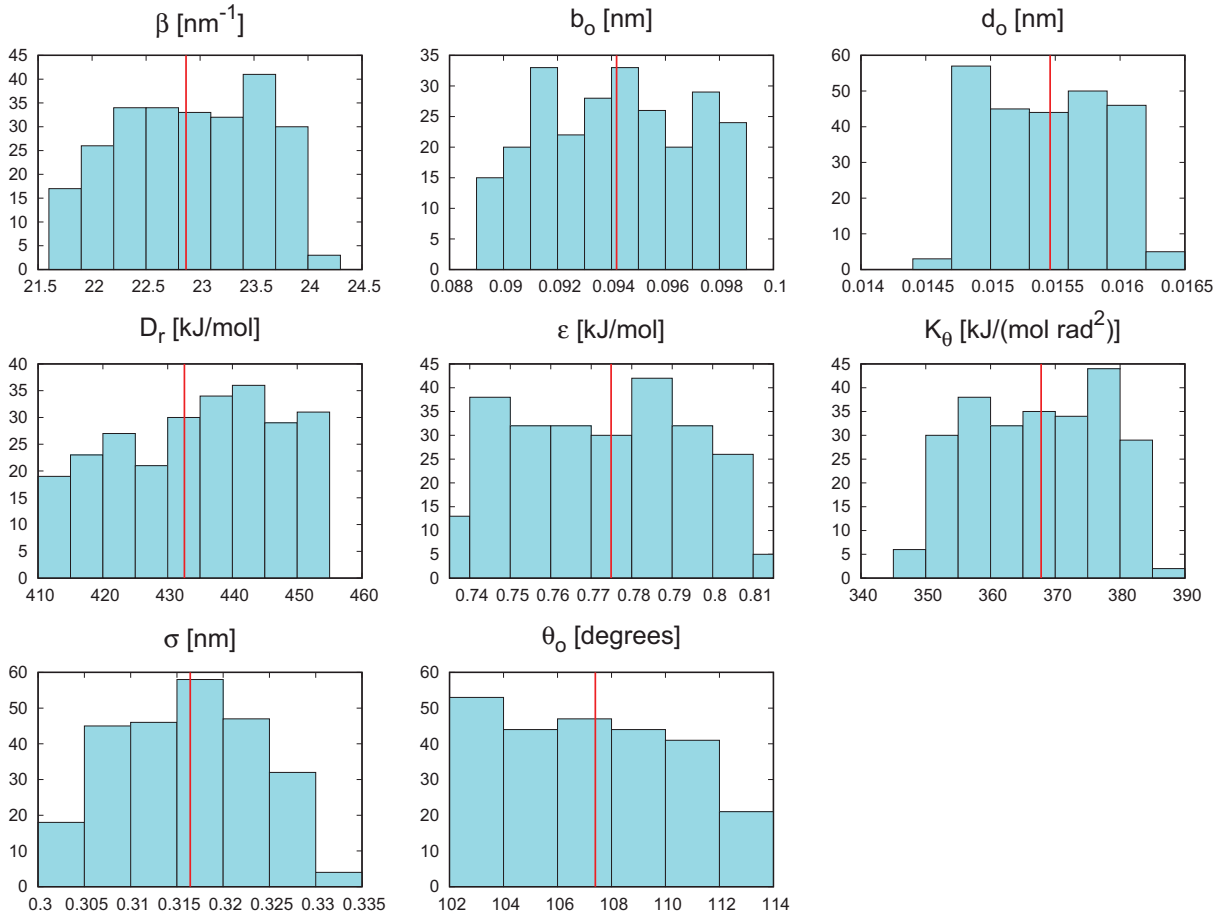
⊗ANS

Fig. 4. Frequency plots of the TIP4P/2005f parameters. The red line corresponds to the published values of the parameters from Gonzlez and Abascal.[25]
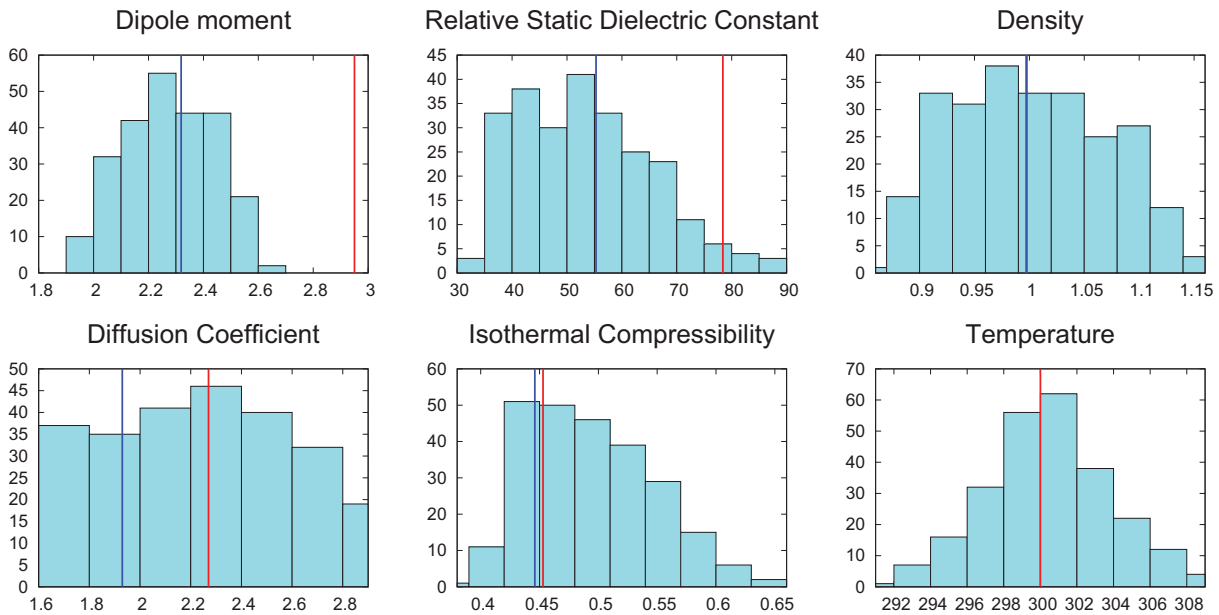

Fig. 5. Frequency plots of thermophysical properties. Red lines are the experimental values, and blue lines are the values listed in Ref. 25.
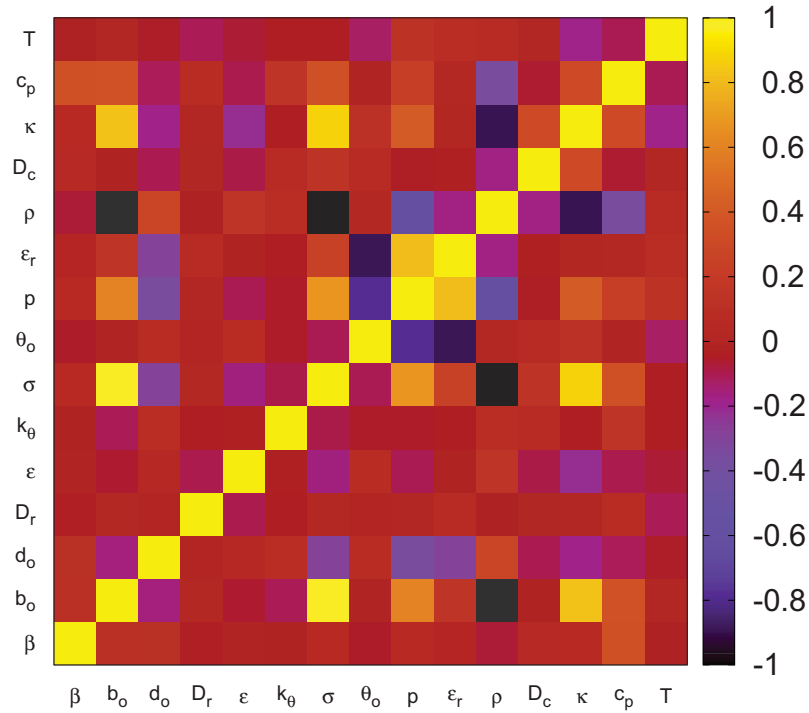
Fig. 6. Correlation matrix of the TIP4P/2005f model parameters and thermophysical properties.

TABLE V

Correlation Matrix of the TIP4P/2005f Parameters

	β	b_0	d_0	D_r	ϵ	k_θ	σ	θ_0
β	1.000							
b_0	0.106	1.000						
d_0	0.092	−0.163	1.000					
D_r	−0.041	0.024	−0.005	1.000				
ϵ	−0.010	−0.061	0.031	−0.099	1.000			
k_θ	−0.023	−0.109	0.097	−0.046	−0.029	1.000		
σ	0.063	0.969	−0.286	0.022	−0.164	−0.095	1.000	
θ_0	−0.055	−0.017	0.090	−0.006	0.089	−0.054	−0.104	1.000

values than the published values. This is expected since the diffusion coefficient was included in the calculation of the UMC weights, and isothermal compressability is related to density. The spread in the diffusion coefficient is larger than expected given that it was used as a constraint in the UMC weights, likely because the original parameters calculated the diffusion coefficient to be approximately 15% of the experimental value, which is similar to the percent UMC uncertainty calculated in Table IV.

In Fig. 6, very few of the TIP4P/2005f model parameters share a strong cross correlation, except the

hydrogen-oxygen bond length b_0 and the Lennard-Jones distance parameter σ. Aside from including an oxygen atom, no significant reason exists for why these two parameters should relate; the Lennard-Jones distance parameter is an intermolecular component, and the hydrogen-oxygen bond length is intramolecular. Regarding the thermophysical properties, there is a strong correlation between the dipole moment and relative static dielectric constant (p and ϵ_r), which is expected.

Besides these two properties, the most notable cross-correlation terms all involve the density, including the

⊗ANS

anticorrelations between density and the hydrogen-oxygen bond length, Lennard-Jones distance parameter, and isothermal compressibility. The hydrogen-oxygen bond length affects how closely packed the water molecule is, and the Lennard-Jones distance parameter affects how closely packed the neighboring water molecules are to one another, both of which directly impact the density of the system. The isothermal compressibility relates how volume changes with varying pressure, which is strongly dependent on density.

Additionally, the bond angle exhibits a strong anticorrelation with both electrostatic thermophysical properties. Because the bond angle is a component that determines the location of hydrogen atoms, both of which contain a positive charge in the model, the authors expected that the electrostatic terms would be affected. Although there are noticeable correlations between these electrostatic terms and the other distance parameters, the bond angle unexpectedly contains the strongest correlation.

IV.C. Phonon Density of States

The covariance matrix on the phonon density of states can also be calculated using the UMC weights. The mean value of the phonon density of states with a 1-standard-deviation band is shown in Fig. 7. Generally, the uncertainty band below 150 meV is reasonably constrained, which is not the case for the 205- and 430-meV peaks. The large uncertainty bands around these modes are largely due to variations in the peak locations rather than the peak magnitudes, as shown in
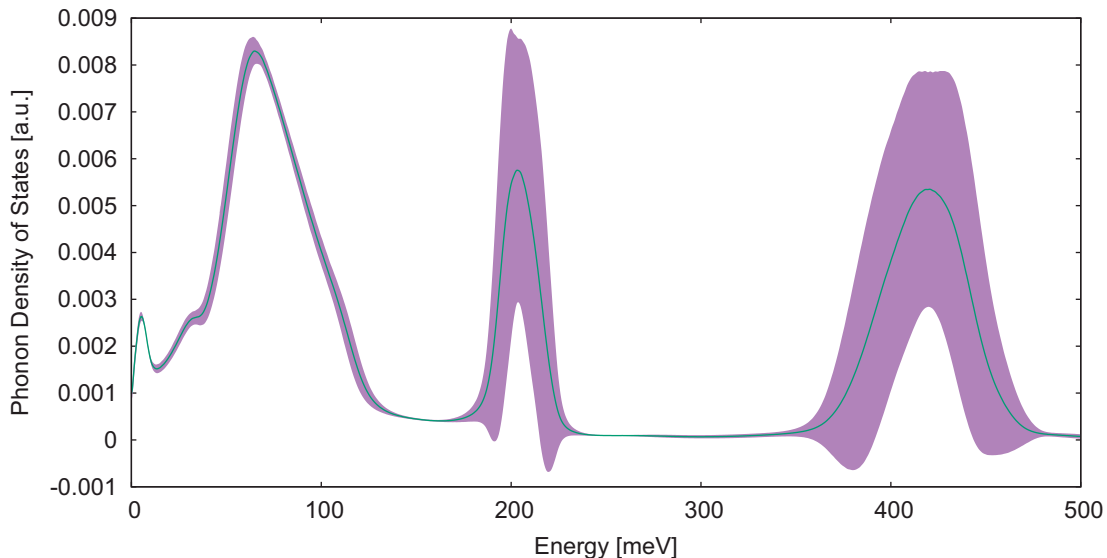
Fig. 8, which shows the 250 phonon density of states from the accepted runs used to calculate the UMC weights. The continuous spectrum (below 150 meV) is consistent between the 250 accepted runs, and the 205-meV modes are fairly consistent across the runs. The 430-meV mode exhibits a wide spread in the energy of the peak locations. These large uncertainties appear in certain quantities but not others, as discussed in Sec. V.

A plot of the correlation matrix is shown in Fig. 9, and the uncertainties around the 205- and 430-meV peaks are clearly significantly larger than the peaks below 150 meV. Interestingly, there is a noticeable dip in the overall uncertainty at the actual peak values and an increase in uncertainty immediately surrounding them. This is validation that the location of these modes is well known, whereas the peak width is more uncertain. In other nuclear data processing codes [e.g., NJOY], these higher energy modes are approximated as Dirac delta functions with an associated weight to signify the peak magnitudes. The small relative uncertainties of the mode locations could indicate that approximating the modes as Dirac delta functions is appropriate.

IV.D. Dynamic Structure Factor

A plot of the mean value of the dynamic structure factor $S(q, E)$ is shown in Fig. 10, and its relative uncertainty is shown in Fig. 11. The relative uncertainty plot is capped between 0 and 1 because some values on the edge of the plots are much greater than 1 but correspond to very small values of $S(q, E)$. Overall, the relative
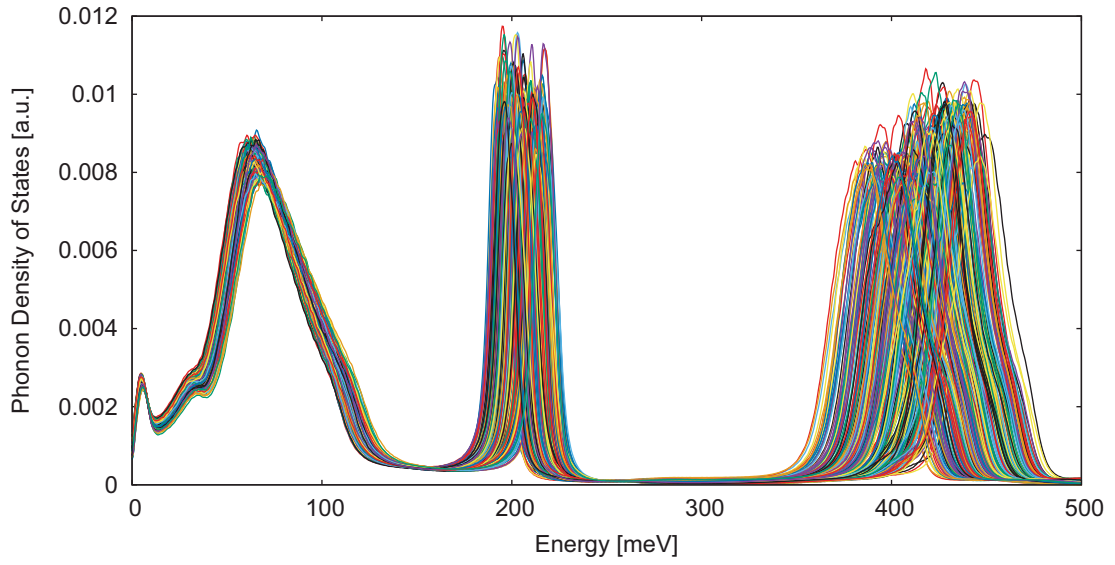

Fig. 7. Phonon density of states with ± 1 standard deviation uncertainty band.

Fig. 8. All accepted phonon density of states used to generate the covariance matrix.
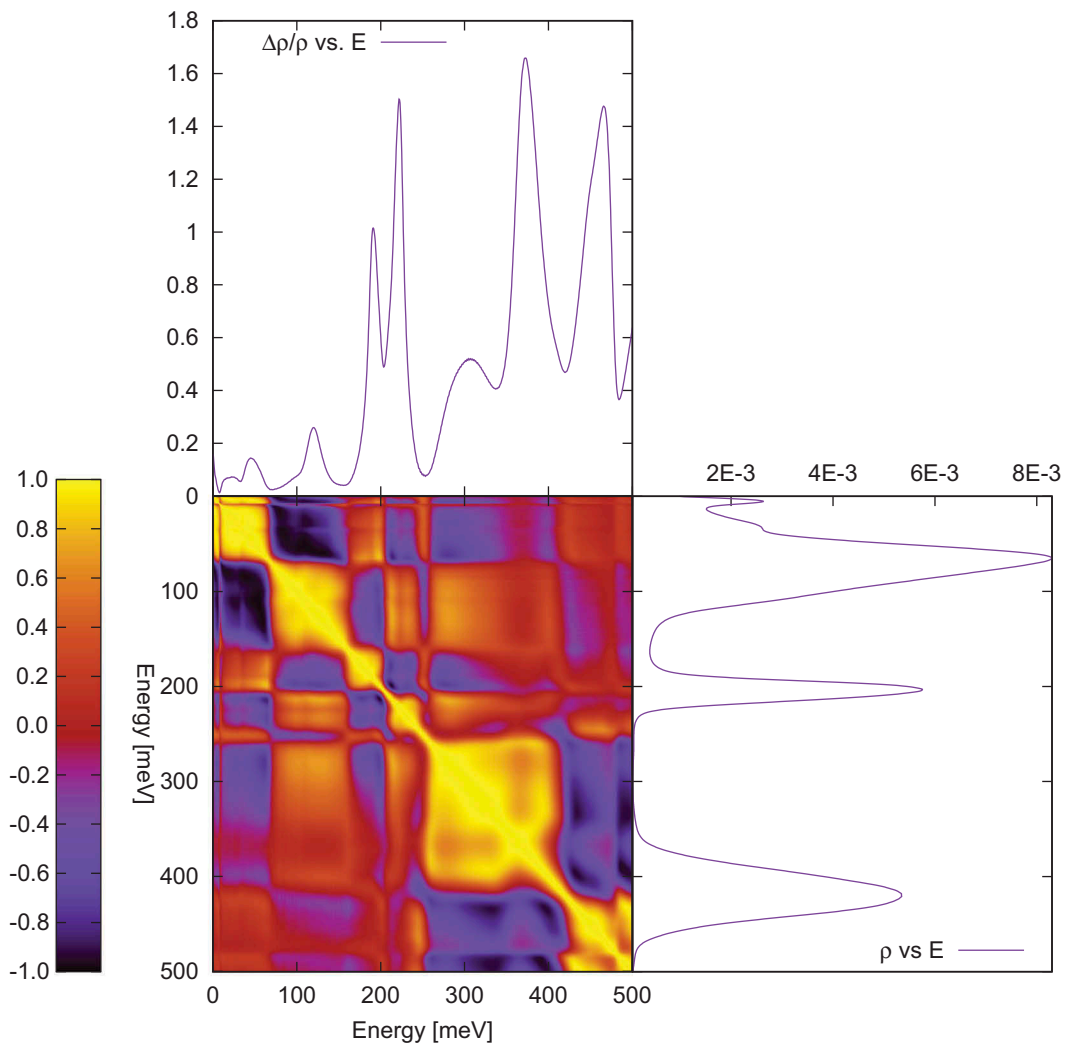

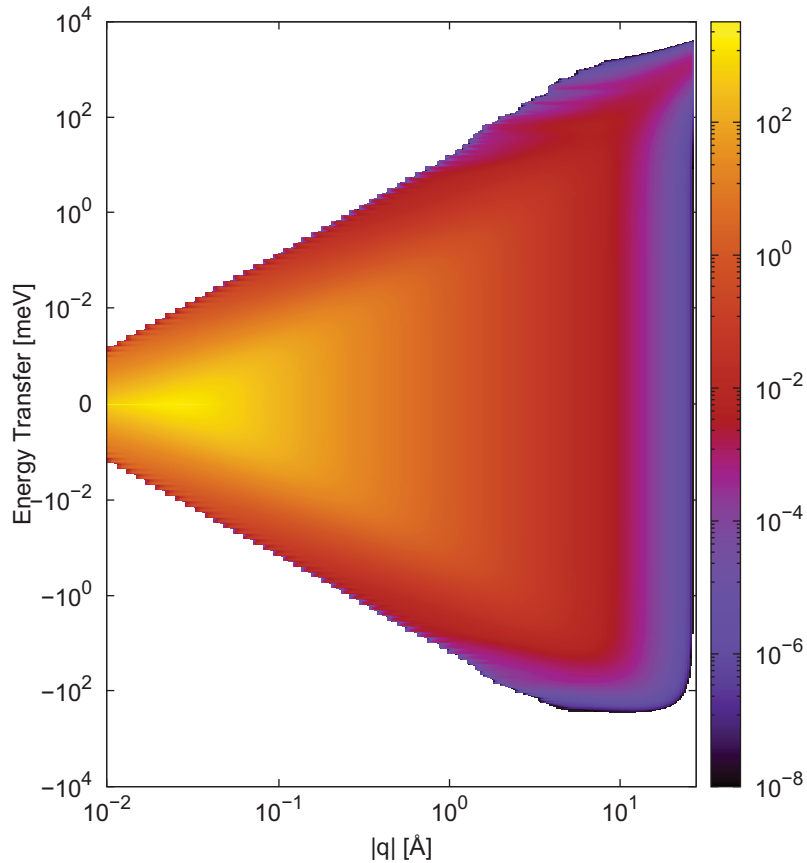Fig. 9. Correlation matrix of phonon density of states.

⊗ANS

Fig. 10. Mean value of $S(q, E)$.

uncertainty is around 0.15, which is near the uncertainty in the phonon density of states below 100 meV. This could indicate that the majority of the uncertainties are dictated by the phonon density of states below the 100- to 150-meV range. The relative uncertainties differ from this in two areas. The first is the two distinct bands that appear in Fig. 11 starting at $q = 0.025 Å^{-1}$. What these dips represent in relative uncertainty is unclear, but the valley moves linearly in energy and quadratically in momentum. This could be related to how the intermediate structure factor is calculated from Eq. (7) since there is a q^2 term in the exponential. However, the relative uncertainties of the intermediate structure factor do not indicate that it would manifest in the dynamic structure factor. Additionally, there are noticeable increases in relative uncertainty that occur around 205 and 430 meV from the increased uncertainties in the phonon density of states mentioned previously.

IV.E. Double-Differential Cross Section

Plots of the double-differential cross section for various incident energies and scattering angles, as well as the relative uncertainty between the ORNL evaluation and experimental data, are shown in Fig. 12. The green band represents the ORNL evaluation with ± 1 standard deviation from the mean. Overall, both the ENDF/B-VIII.0 and the new ORNL evaluation agree somewhat favorably with the experimental data near the quasielastic peaks, but there are disagreements near the tails of the double-differential cross sections. The large spikes in relative uncertainty correspond to uncertainties in the phonon density of states. Because these spikes do not correspond to an increase in uncertainty in the experimental results, there could be a bias in the model toward being more sensitive to the translational and vibrational modes of water than to the double-differential data used to generate the UMC weights.

Interestingly, the intensity of the relative uncertainties is not consistent across different double-differential cross sections. For example, when the energy transfer is 50 meV, the relative uncertainty is around 0.125 for $E_i = 160$ meV, 0.325 for $E_i = 250$ meV, and 0.1 for $E_i = 600$ meV. This contrasts with the uncertainty at the elastic peak at which the energy
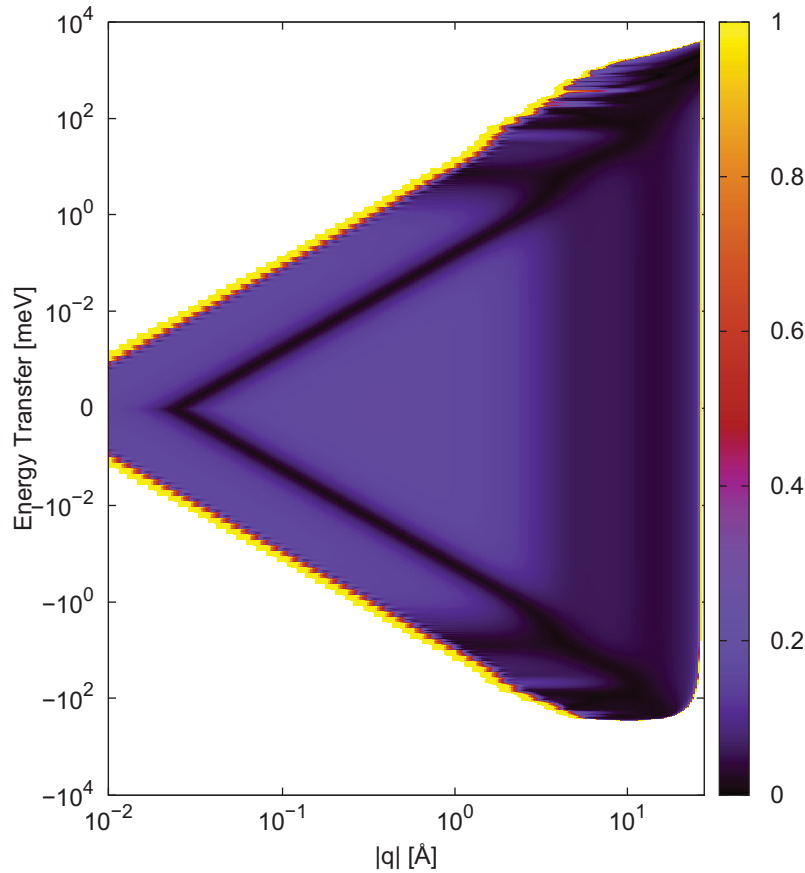
Fig. 11. Relative uncertainty of $S(q, E)$. The intensity is limited to 1 because there are some large relative uncertainties on the edges of the plot that also correspond to very small values of $S(q, E)$.

transfer = 0, which is close to 0.05 for all four incident energies.

IV.F. Total Cross Section

Plots of the scattering cross section and the UMC-generated relative uncertainty are shown in Fig. 13. Although there are independent experimental values of the total cross section of water at thermal energies, they are not at the same temperature as the scattering experiment (300 K), and therefore are not shown here. The UMC-generated cross section is slightly larger than the ENDF/B-VIII.0 evaluation below 0.05 eV with a slight increase around 1 eV. The relative uncertainties, unlike with the dynamic structure factor and double-differential cross sections, do not show any significant dependence on the 205- or 430-meV peaks from the phonon density of states. Instead, the relative uncertainties tend to be largest where the cross section diverges from the ENDF/B-VIII.0 value, including a small increase in uncertainty

corresponding to the small increase in cross section at 1 eV. The increased relative uncertainties at 30 and 360 meV are unusual, and it is unclear if they correspond to any physical phenomena. Previous work[3] suggests the increase at 360 meV may be due to the uncertainty associated with the 430-meV peak from the phonon density of states.

V. TESTING

To test the new thermal scattering cross section and covariance, several critical benchmarks were simulated. Because the experiment was conducted at 300 K, higher temperature benchmarks were preferred. This preference and the need for a thermal spectrum meant only a handful of benchmarks from the ICSBEP Handbook[8] could be considered. Experiments LCT-078, LCT-079, and LCT-080 were chosen because they were performed at 298 K, 300 K, and 298 K, respectively. LCT-078 and LCT-080 are part of the Seven Percent Critical Experiment
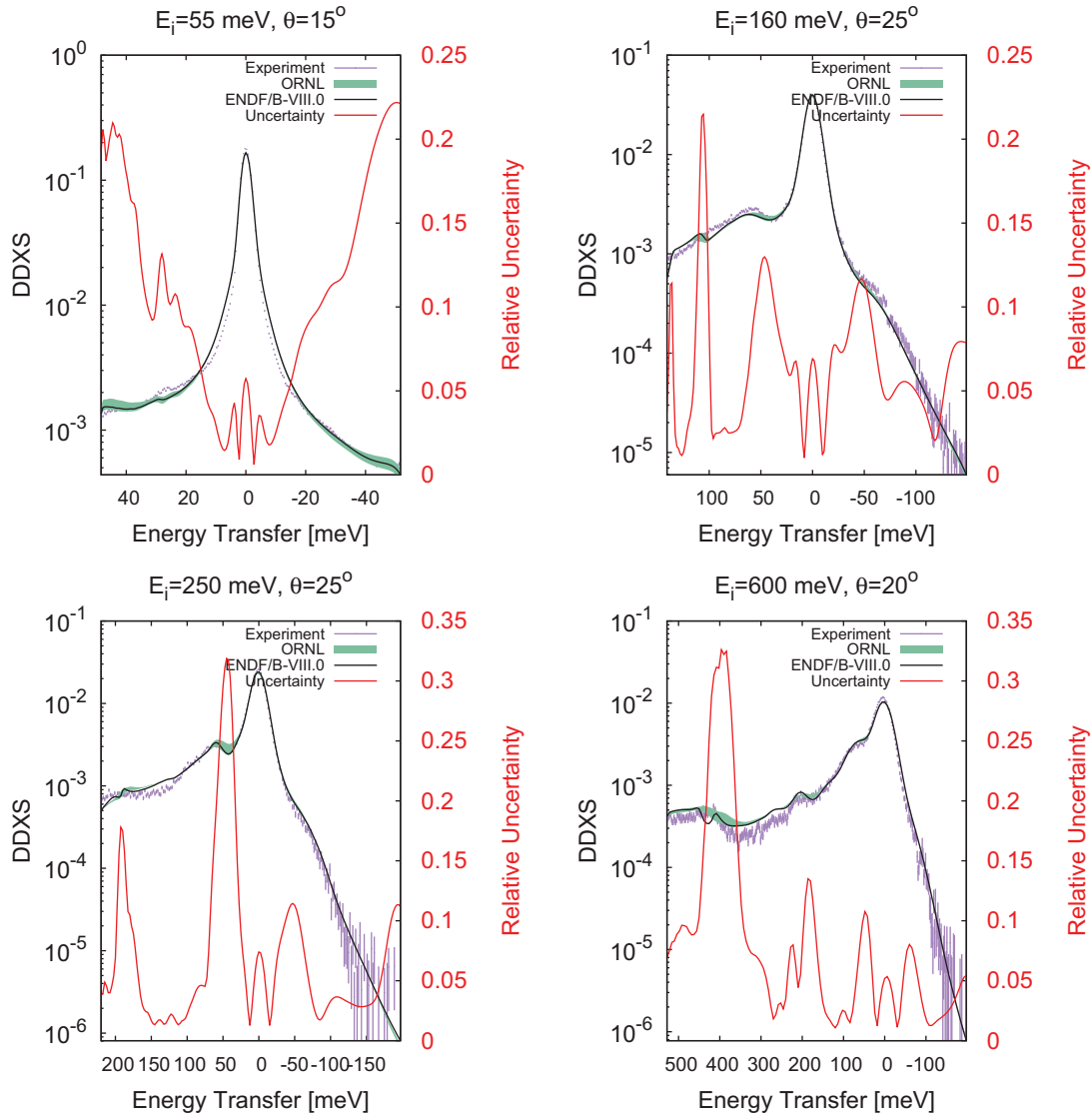
Fig. 12. Double-differential cross sections at various incident energies and scattering angles. The bands represent the mean value ± 1 standard deviation of the UMC-calculated values.

performed at Sandia National Laboratories for which the fuel was arranged in square-pitched arrays with different pitches for the two sets of experiments. LCT-079 is part of the Burnup Credit Critical Experiment at Sandia National Laboratories and contains triangular-pitched fuel rods.

An updated library of light water was generated using the mean value of the dynamic structure factor shown in Sec. II.A. A plot comparing the benchmark results against simulations run using the ENDF/B-VIII.0 library of water and this updated library of water is shown in Fig. 14. The simulations were run using MCNP6.2, and all the cross sections were processed using NJOY21. The error bars on the benchmark bars indicate the benchmark uncertainties,

and the error bars on the ENDF/B-VIII.0 and ORNL bars indicate statistical uncertainties from the MCNP simulations (i.e., they do not incorporate uncertainties in the nuclear data).

Overall, the new library agrees very favorably with the ENDF/B-VIII.0 library. This is expected because the methods for generating the libraries are similar. The new library performs slightly better than the ENDF/B-VIII.0 library, but the improvement is usually negligible.

Although this analysis validates the mean value, it does not validate the generated covariance matrices. Ideally, the spread of the data generated from the covariance matrix should match the spread of the data used to generate the covariance matrix. To validate the
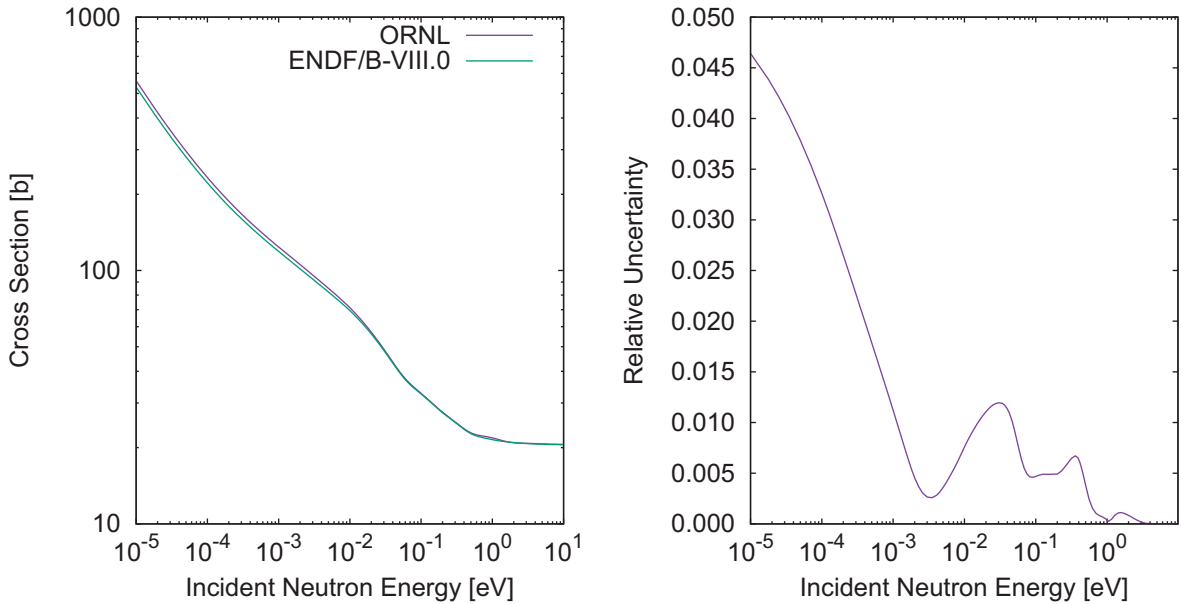
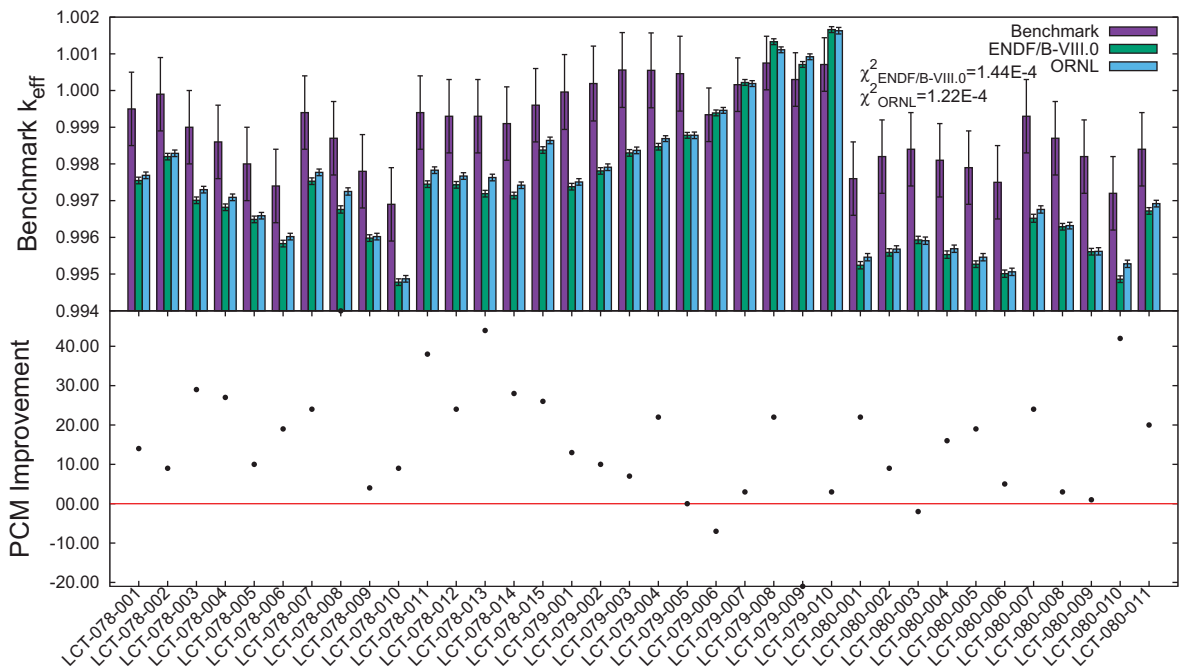Fig. 13. Scattering cross section for hydrogen in H_2O.

Fig. 14. Benchmark comparison between ENDF/B-VIII.0- and UMC-generated thermal scattering libraries.

covariance matrix methodology, the phonon density of states covariance matrix was used to generate 250 random phonon density of states. Phonon density of states were chosen instead of the thermal scattering law for several reasons. First, there is a direct relation from phonon density of states to the thermal scattering law due to the incoherent approximation outlined in Eqs. (5), (6), and (7), so it should be possible to capture all

the physics of thermal neutron scattering within the phonon density of states. Additionally, a full covariance matrix of the thermal scattering law would be on the order of 40 GB, which is too large to store in memory and quickly sample. Finally, because there is no agreed-upon method for storing the covariance matrices of thermal scattering cross sections, it would serve as a possibility for storing covariance information in
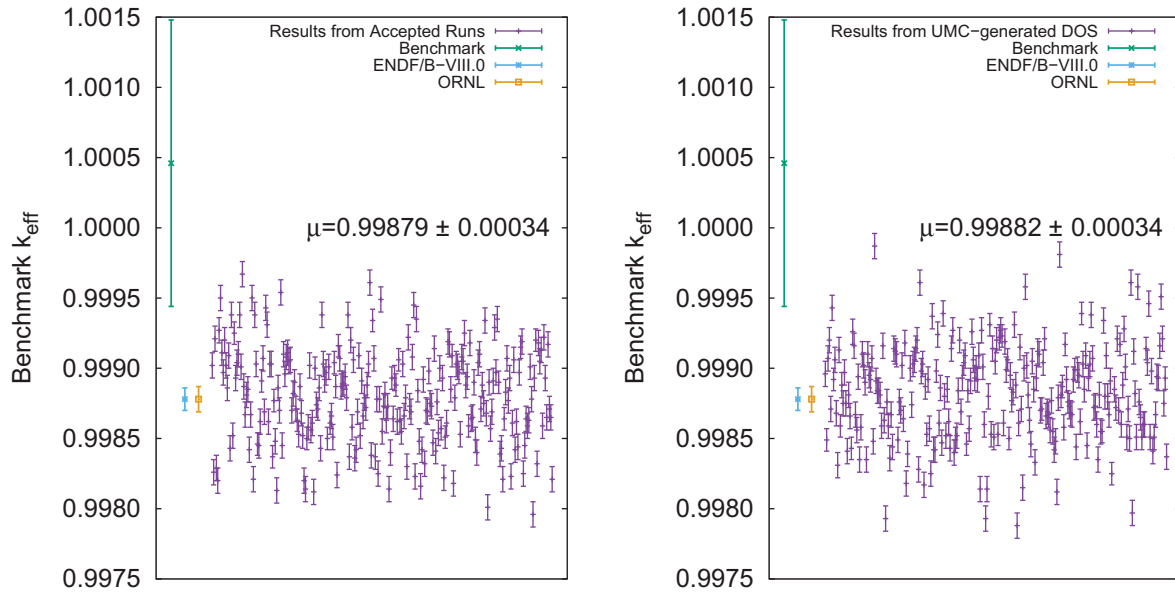
⊗ANS

Fig. 15. Spread of k_{eff} using (a) the 250 phonon density of states used to generate covariance matrix, and (b) the 250 phonon density of states sampled from covariance matrix.

materials that are traditionally evaluated using the incoherent approximation.

These 250 phonon density of states were transformed into the requisite dynamic structure factor to be compared against benchmark results. The accepted phonon density of states used to calculate the UMC weights were used as a baseline to compare against these newly generated phonon density of states. The results of these runs for one of the benchmarks (LCT-079-005) is shown in Fig. 15.

The text labeled μ describes the mean value of the 250 runs, either accepted runs or UMC-generated runs, and gives their 1-standard-deviation spread. Not only do both cases have very similar mean values, but they also have an identical standard deviation, indicating that the covariance matrix of the phonon density of states might be a memory-saving method for describing the spread of uncertainty of the thermal scattering law as opposed to requiring the covariance matrix of the full $S(\alpha, \beta)$.

VI. CONCLUSION

A methodology for evaluating thermal neutron scattering cross sections was developed. Using the UMC method to compare experimentally measured double-differential scattering cross sections against computational simulations, this work generated optimized values of the TIP4P/2005f potential parameter set, phonon density of states, thermal scattering law, double-differential

scattering cross sections, and total scattering cross sections of light water. The updated model parameters were found to have a maximum of 0.54% relative error from the published values, which is well within the UMC-calculated uncertainties on the order of 2.7%, and the double-differential cross sections agreed favorably with ENDF/B-VIII.0 cross sections. Covariance matrices of the parameter set, thermophysical properties, and phonon density of states were also generated. The mean values of the thermal scattering law and covariance matrix of the phonon density of states were compared against ICSBEP benchmarks and found to be in good agreement with experimental results and a slight improvement over the ENDF/B-VIII.0 data set.

The uncertainties present in the double-differential scattering cross section and total cross section could be reduced. The TIP4P/2005f parameters were initially sampled assuming no correlations to one another. Including the calculated correlations from the lower-left 8×8 square in Fig. 6 might reduce the overall uncertainties. Additionally, including experimental cross sections in the calculation of the UMC weights could reduce or remove the uncertainty found in Fig. 13.

In addition to the TIP4P/2005f parameters, other physical parameters describing water could be included in the sampling. Of note is the free-atom scattering cross section. This could prove influential as Ref. 3 has concluded, but since there are predefined uncertainties in this value,[9] this would serve as a bound to the sampling phase space.

As previously mentioned, there is no agreed-upon method to address the large memory footprint of a full thermal scattering covariance matrix. These issues are being addressed in various WPEC subgroups, and we look forward to incorporating those methods in future iterations of this work. The methods range from storing the covariance matrix as a groupwise $S(\alpha, \beta)$ to implementing the iterated fission probability method for calculating sensitivities.

The method used to validate the covariance matrix is not analogous to how covariance data are validated for the resonance region or fast region cross sections because current neutron transport code systems are not equipped to handle thermal scattering covariance matrices. This work was done partially to promote the development of such capabilities in future transport code systems. Additionally, once a method for storing covariance matrices of thermal scattering law data is developed, comparing the spread in the results from that method to the one described in this work will be interesting.

Supplemental Data

Supplemental data for this article can be accessed online—see DOI on the title page.

Acknowledgments

ORCID

Chris W. Chapman http://orcid.org/0000-0001-9222-0075

REFERENCES

1. J. C. HOLMES, A. I. HAWARI, and M. L. ZERKLE, "A Phonon-Based Covariance Methodology for ENDF S (α, β) and Thermal Neutron Inelastic Scattering Cross Sections," *Nucl. Sci. Eng.*, **184**, *1*, 84 (2016); https://doi.org/10.13182/NSE15-89.

2. R. MacFARLANE and A. KAHLER, "Methods for Processing ENDF/B-VII with NJOY," Nucl. Data Sheets, **111**, *12*, 2, 739 (2010); https://doi.org/10.1016/j.nds.2010.11.001.

3. L. MAUL, "Thermal Scattering Law Uncertainties and Propagation into Small Thermal Fission Reactors," PhD Dissertation, University of New South Wales (2018).

4. G. NOGUERE et al., "Covariance Matrices of the Hydrogen Neutron Cross Sections Bound in Light Water for the JEFF-3.1.1 Neutron Library," *Ann. Nucl. Energy*, **104**, 132 (2017); https://doi.org/10.1016/j.anucene.2017.01.044.

5. J. P. SCOTTA, G. NOGUERE, and J. I. MARQUEZ DAMIAN, "Generation of the H-1 in H_2O Neutron Thermal Scattering Law Covariance Matrix of the CAB Model," *EPJ Nucl. Sci. Technol.*, **4**, 32 (2018); https://doi.org/10.1051/epjn/2018024.

6. V. D. SPOEL et al., "GROMACS: Fast, Flexible, and Free," *J. Comput. Chem.*, **26**, *16*, 1,701 (2005); https://doi.org/10.1002/jcc.20291.

7. J. GOORLEY et al., "Initial MCNP6 Release Overview," LA-UR-13-22934, Los Alamos National Laboratory (2013).

8. "International Handbook of Evaluated Criticality Safety Benchmark Experiments," NEA/NSC/DOC(95)03, Nuclear Science Committee, Nuclear Energy Agency (2017).

9. D. L. PRICE and F. FERNANDEZ-ALONSO, *Neutron Scattering - Fundamentals*, Academic Press (2013).

10. G. SQUIRES, *Thermal Neutron Scattering*, Cambridge University Press (1978).

11. L. VAN HOVE, "Correlations in Space and Time and Born Approximation Scattering in Systems of Interacting Particles," *Phys. Rev.*, **95**, *1*, 249 (1954); https://doi.org/10.1103/PhysRev.95.249.

12. I. I. GUREVICH and L. V. TARASOV, *Low-Energy Neutron Physics*, North Holland Publishing Company (1968).

13. V. JAISWAL and L. LEAL, "Investigation of Frequency Spectrum of Light Water to Generate Thermal Scattering Law" (2018).

14. C. A. MANRING and A. I. HAWARI, "Assessment of Thermal Neutron Scattering in a Heavy Paraffinic Molecular Material," *Ann. Nucl. Energy*, **128**, 140 (2019); https://doi.org/10.1016/j.anucene.2018.12.042.

⊗ANS

15. F. FRÖHNER, "Evaluation and Analysis of Nuclear Resonance Data," JEFF Report 18, Nuclear Energy Agency/Organisation for Economic Co-Operation and Development (2000).

16. M.-G. KIM, H.-L. JANG, and S. CHO, "Adjoint Design Sensitivity Analysis of Reduced Atomic Systems Using Generalized Langevin Equation for Lattice Structures," *J. Comput. Phys.*, **240**, 1 (2013); https://doi.org/10.1016/j.jcp.2013.01.020.

17. D. L. SMITH, "Covariance Matrices for Nuclear Cross Sections Derived from Nuclear Model Calculations," (ANL/NDM—159). United States (January 2005); https://doi.org/10.2172/838257.

18. D. SMITH, "A Unified Monte Carlo Approach to Fast Neutron Cross Section Data Evaluation," (ANL/NDM—166). United States (March 2008); https://doi.org/10.1002/9780470995327.ch266.

19. R. CAPOTE and D. SMITH, "An Investigation of the Performance of the Unified Monte Carlo Method of Neutron Cross Section Data Evaluation," *Nucl. Data Sheets*, **109**, 12, 2768 (2008); https://doi.org/10.1016/j.nds.2008.11.007.

20. D. SMITH, *Probability, Statistics and Data Uncertainties in Nuclear Science and Technology*, American Nuclear Society (1991).

21. R. CAPOTE et al., "A New Formulation of the Unified Monte Carlo Approach (UMC-B), and Cross-Section Evaluation for the Dosimetry Reaction ^{55}Mn(n, γ)^{56}Mn," *J. ASTM Int.*, **9**, 3, 1 (2012).

22. G. SCHNABEL, "Large Scale Bayesian Nuclear Data Evaluation with Consistent Model Defects," PhD Dissertation, Technischen Universität Wien Fakultät für Physik (2015).

23. J. OUYANG and R. BETTENS, "Modelling Water: A Lifetime Enigma," *CHIMIA Int. J. Chem.*, **69**, 3, 104 (2015); https://doi.org/10.2533/chimia.2015.104.

24. "Four site water model," (accessed December 3, 2019); http://www.sklogwiki.org/SklogWiki/index.php/File:Four_site_water_model.png.

25. M. GONZÁLEZ and J. ABASCAL, "A Flexible Model for Water Based on TIP4P/2005," *J. Chem. Phys.*, **26**, 22, 224516 (2011); https://doi.org/10.1063/1.3663219.

26. J. MARQUEZ DAMIAN, D. MALASPINA, and J. GRANADA, "CAB Models for Water: A New Evaluation of the Thermal Neutron Scattering Laws for Light and Heavy Water in ENDF-6 Format," *Ann. Nucl. Eng.*, **65**, 280 (2014); https://doi.org/10.1016/j.anucene.2013.11.014.

27. T. DARDEN, D. YORK, and L. PEDERSEN, "Particle Mesh Ewald: An $N \cdot \log(N)$ Method for Ewald Sums in Large Systems," *J. Chem. Phys.*, **98**, 12, 10089 (1993); https://doi.org/10.1063/1.464397.

28. G. E. GRANROTH et al., "SEQUOIA: A Newly Operating Chopper Spectrometer at the SNS," *J. Phys. Conf. Ser.*, **251**, 012058 (2010).

29. C. W. CHAPMAN, "Thermal Neutron Scattering Evaluation Methodology," PhD Dissertation, Nuclear & Radiological Engineering & Medical Physics, Georgia Institute of Technology (2017).

30. G. ARBANAS et al., "Bayesian Optimization of Generalized Data," *EPJ Nuclear Sci. Technol.*, **4**, 30 (2018); https://doi.org/10.1051/epjn/2018038.